2006

Prediction and diagnosis of Tropical Cyclone formation in an NWP system. Part II

Tory, K. J

Prediction and Diagnosis of Tropical Cyclone Formation in an NWP System. Part II: A Diagnosis of Tropical Cyclone Chris Formation

K. J. TORY

Bureau of Meteorology Research Centre, Melbourne, Victoria, Australia

M. T. MONTGOMERY

Department of Meteorology, Naval Postgraduate School, Monterey, California, and Hurricane Research Division, NOAA/AOML, Miami, Florida

N. E. DAVIDSON AND J. D. KEPERT

Bureau of Meteorology Research Centre, Melbourne, Victoria, Australia

(Manuscript received 16 November 2004, in final form 5 January 2006)

ABSTRACT

This is the second of a three-part investigation into tropical cyclone (TC) genesis in the Australian Bureau of Meteorology's Tropical Cyclone Limited Area Prediction System (TC-LAPS). The primary TC-LAPS vortex enhancement mechanism (convergence/stretching and vertical advection of absolute vorticity in convective updraft regions) was presented in Part I. In this paper (Part II) results from a numerical simulation of TC Chris (western Australia, February 2002) are used to illustrate the primary and two secondary vortex enhancement mechanisms that led to TC genesis. In Part III a number of simulations are presented exploring the sensitivity and variability of genesis forecasts in TC-LAPS.

During the first 18 h of the simulation, a mature vortex of TC intensity developed in a monsoon low from a relatively benign initial state. Deep upright vortex cores developed from convergence/stretching and vertical advection of absolute vorticity within the updrafts of intense bursts of cumulus convection. Individual convective bursts lasted for 6–12 h, with a new burst developing as the previous one weakened. The modeled bursts appear as single updrafts, and represent the mean vertical motion in convective regions because the 0.15° grid spacing imposes a minimum updraft scale of about 60 km. This relatively large scale may be unrealistic in the earlier genesis period when multiple smaller-scale, shorter-lived convective regions are often observed, but observational evidence suggests that such scales can be expected later in the process. The large scale may limit the convection to only one or two active bursts at a time, and may have contributed to a more rapid model intensification than that observed.

The monsoon low was tilted to the northwest, with convection initiating about 100–200 km west of the low-level center. The convective bursts and associated upright potential vorticity (PV) anomalies were advected cyclonically around the low, weakening as they passed to the north of the circulation center, leaving remnant cyclonic PV anomalies.

Strong convergence into the updrafts led to rapid ingestion of nearby cyclonic PV anomalies, including remnant PV cores from decaying convective bursts. Thus convective intensity, rather than the initial vortex size and intensity, determined dominance in vortex interactions. This scavenging of PV by the active convective region, termed diabatic upscale vortex cascade, ensured that PV cores grew successively and contributed to the construction of an upright central monolithic PV core. The system-scale intensification (SSI) process active on the broader scale (300–500-km radius) also contributed. Latent heating slightly dominated adiabatic cooling within the bursts, which enhanced the system-scale secondary circulation. Convergence of low- to midlevel tropospheric absolute vorticity by this enhanced circulation intensified the system-scale vortex. The diabatic upscale vortex cascade and SSI are secondary processes dependent on the locally enhanced vorticity and heat respectively, generated by the primary mechanism.

Corresponding author address: K. J. Tory, Bureau of Meteorology Research Centre, GPO Box 1289, Melbourne, VIC, 3001, Australia.
E-mail address: k.tory@bom.gov.au

1. Introduction

It has been known for more than half a century that tropical cyclone (TC) formation requires intense convection in an environment of sufficient absolute vorticity and humidity (e.g., Gray 1998 and references therein). The underlying thermomechanical processes responsible for the construction of these intense mesoscale vortices, however, has been and remains very much under debate. Tory et al. (2006, hereafter Part I) noted that the genesis theories of Simpson et al. (1997), Ritchie and Holland (1997), and Bister and Emanuel (1997) focused almost entirely on vortex enhancement in the stratiform precipitation region of mesoscale convective systems (MCSs). The stratiform divergence profile (SDP) enhances the absolute vorticity magnitude in the middle troposphere and weakens it above and below. Hereafter we refer to this as stratiform vortex enhancement (SVE). These authors suggested that genesis was a process that brings the abundant midlevel vorticity down to the surface, and proposed various mechanisms to achieve this. In contrast, Montgomery and Enagonio (1998) considered vortex enhancement in MCS deep convective regions as a means for generating the low-level cyclonic vorticity necessary for genesis. The convective divergence profile (CDP) increases the magnitude of absolute vorticity in the lower troposphere and reduces it in the upper troposphere, hereafter referred to as convective vortex enhancement (CVE).

More recent modeling studies (Hendricks et al. 2004, hereafter H04; Montgomery et al. 2006, hereafter M06) have found CVE to be critical for genesis. In Part I the primary vortex enhancement mechanism in a simulation of the genesis of TC Chris was shown to be CVE. These studies do not suggest SVE plays no role in genesis, only that CVE is critical for genesis. In Part I it was noted that sufficient observations do not currently exist to prove conclusively the critical role of CVE in genesis. However, observational evidence was recalled that show relatively large areas (30 km and greater) of CDP often exist in the tropical oceanic atmosphere, and intense convective bursts on the same scale exhibiting very cold cloud-top temperatures suggestive of overshooting in vigorous convection are frequently observed in developing TCs. The CVE process produces vortex cores that extend from the low to mid levels of the troposphere, through convergence/stretching of absolute vorticity in convective updrafts. Vertical advection of absolute vorticity also plays a role in the upward growth of the vortex core. This mechanism was termed the primary vortex enhancement mechanism in Part I.

In this current paper (the second of three parts) the secondary vortex enhancement mechanisms, upscale vortex cascade, and the system-scale intensification (SSI) process, introduced by H04 and M06, are shown to be responsible for the construction of a monolithic cyclonic vortex in the TC-LAPS simulation of TC Chris. The primary vortex enhancement mechanism leads to the generation of intense vortex cores on the scale of the model updrafts that fuel the secondary enhancement mechanisms by providing "seed" vortices for the upscale vortex cascade, and provides net heating to drive the system-scale circulation, which converges absolute vorticity at low to mid levels on scales of hundreds of km (the SSI process).

As noted by Gray (1998) there are many wrong ways to the right answer when it comes to TC formation in numerical models. However, if a model has good success forecasting both developing and nondeveloping systems then it is likely to be capturing the most important aspects of TC genesis. Thus our present goal is for qualitative forecast skill (i.e., successful forecasts of development and nondevelopment). Model verification is included to provide some insight into the quantitative model performance, for this particular forecast, and to provide an indication of the processes that appear to be captured by the model and those that are not. The main emphasis of this paper, however, is on documenting the genesis process in TC-LAPS rather than analyzing the forecast skill.

The variability and sensitivity of the TC-LAPS genesis process is investigated in Tory et al. (2005, manuscript submitted to *J. Atmos. Sci.,* hereafter Part III), where additional simulations of developing and nondeveloping storms are presented. The operational NWP model used in this study, TC-LAPS, has been described in Part I, and only a brief description of the model will be provided here. It is hydrostatic on a latitude–longitude grid with horizontal grid spacing of 0.15°. It uses the terrain following σ coordinate in the vertical with 29 levels. The Miller–Pearce time-stepping scheme is combined with a third-order upwinding advection scheme, implemented on an Arakawa A grid (nonstaggered). A state-of-the-art first-order closure boundary layer parameterization scheme is employed, as well as the Tiedke mass–flux scheme for parameterization of convection. A two-step dynamic initialization scheme is used to provide the initial state. First, four consecutive 6-h assimilation cycles are performed to provide target analyses at 6-hourly intervals during the 24-h initialization period. Then a 24-h forecast is run in which dynamical nudging is used to grow a numerically consistent and balanced initial state by nudging the forecast toward the target analyses. During this, artificial heat sources are used to force convection where convection

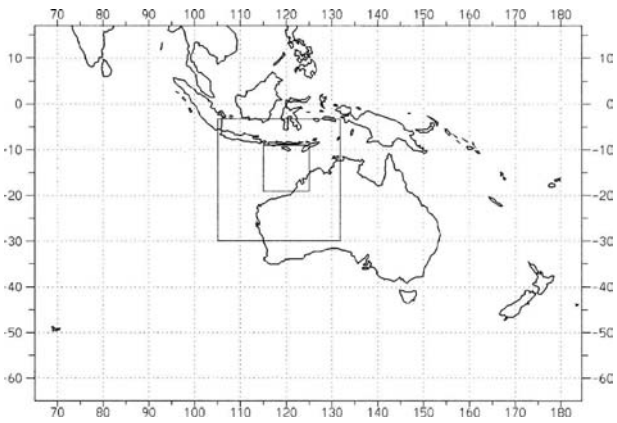

FIG. 1. LAPS375 domain, with the TC Chris TC-LAPS domain embedded. The innermost rectangle represents the subdomain featured in Figs. 4 and 5.

is observed, using remotely sensed cloud-top temperature data. The TC-LAPS domain nested in the Australian Bureau of Meteorology's regional forecast model (LAPS; Puri et al. 1998) for the simulation of TC Chris is shown in Fig. 1.

The remainder of the paper is organized as follows. TC Chris, which formed off the western Australian coast in early February 2002, is introduced in section 2, and model verification is provided using satellite imagery and scatterometer data. The TC-LAPS genesis processes are described and analyzed in detail in section 3 (vortex upscale cascade) and section 4 (SSI), and a summary of the main findings from this work is provided in section 5.

2. TC Chris: Observations and model verification

a. Background

Tropical Cyclone Chris developed in a monsoon depression over the Timor Sea (see Fig. 2a for location) on 3 February 2002. The synoptic environment at 850 hPa over the five days leading up to the TC-LAPS initialization time (1100 UTC 1 February 2002) is illustrated in Fig. 2. On 27 January (Fig. 2a) no significant monsoon trough or westerly flow was present over Indonesia and northern Australia. The easterly trade winds over the Indian Ocean were also weak. Two days later enhanced cross-equatorial flow and monsoon westerlies began to develop, particularly between 100° and 120°E (Fig. 2b). The trade winds over the Indian Ocean also began to strengthen and a cyclonic circulation developed in the shear zone between the monsoon westerlies and easterly trade winds (labeled L in Fig. 2b). Two days later (1100 UTC 31 January 2002), this near-stationary cyclonic circulation had intensified (Fig. 2c) and the downstream ridge to its east also strengthened (labeled H in Fig. 2c). The gray L in Fig. 2c marks the future position of the next cyclone in the eastward developing wave train. By 1100 UTC 1 February 2002, this cyclonic circulation became the monsoon depression that TC Chris subsequently developed in (labeled L in Fig. 2d). This eastward development of successive cyclonic and anticyclonic flows is consistent with the downstream development mechanism described by Davidson and Hendon (1989). During this time there was also evidence of an eastward propagating Madden–Julian oscillation (MJO; not shown) and convection became widespread and active within the monsoon.

The genesis of TC Chris occurred in a low vertical shear region within the monsoon depression during 1–3 February and after reaching TC strength intensified to a category 5 TC [Australian scale, maximum sustained winds >125 kt (64.3 m s^{-1})] within 60 h. The track of TC Chris is shown in Fig. 3. Chris tracked to the south until it made landfall on 7 February.

b. Observations: Satellite images

In Part I it was noted that the convective bursts are likely to be made up of a combination of SDP and CDP, with CDP dominating on average at low levels (i.e., convergence extending from low to mid levels of the troposphere). It is difficult to estimate the scale and intensity of the two precipitation types from satellite imagery and hence the vertical profile of mean horizontal divergence. However, we believe relatively small regions of very cold cloud-top temperatures (CTT) represent significant overshooting in vigorous convective regions. In this study we have found CTT less than 187 K to correlate well with convective rain rates determined from three-hourly-averaged 0.25° resolution Tropical Rainfall Measuring Mission (TRMM) data (not shown), using a rain-rate threshold of 10 mm h^{-1} or greater to identify convective pixels (Rapp et al. 2005). In the following analysis we interpret CTT regions of less than 187 K as convective, dominated by a CDP. Larger areas of weaker but nearly contiguous rainfall were also evident in the TRMM data, consistent with the notion that stratiform and convective regions coexist (Houze 1997).

Figure 4 (left panels) shows infrared satellite images during the genesis period. Where available, scatterometer winds have been overlaid to indicate the position of the low-level circulation. Although all obvious examples of rain-affected scatterometer data have been manually removed from these images, we have not performed a rigorous check of the data since we are only trying to illustrate the general low-level flow pattern.

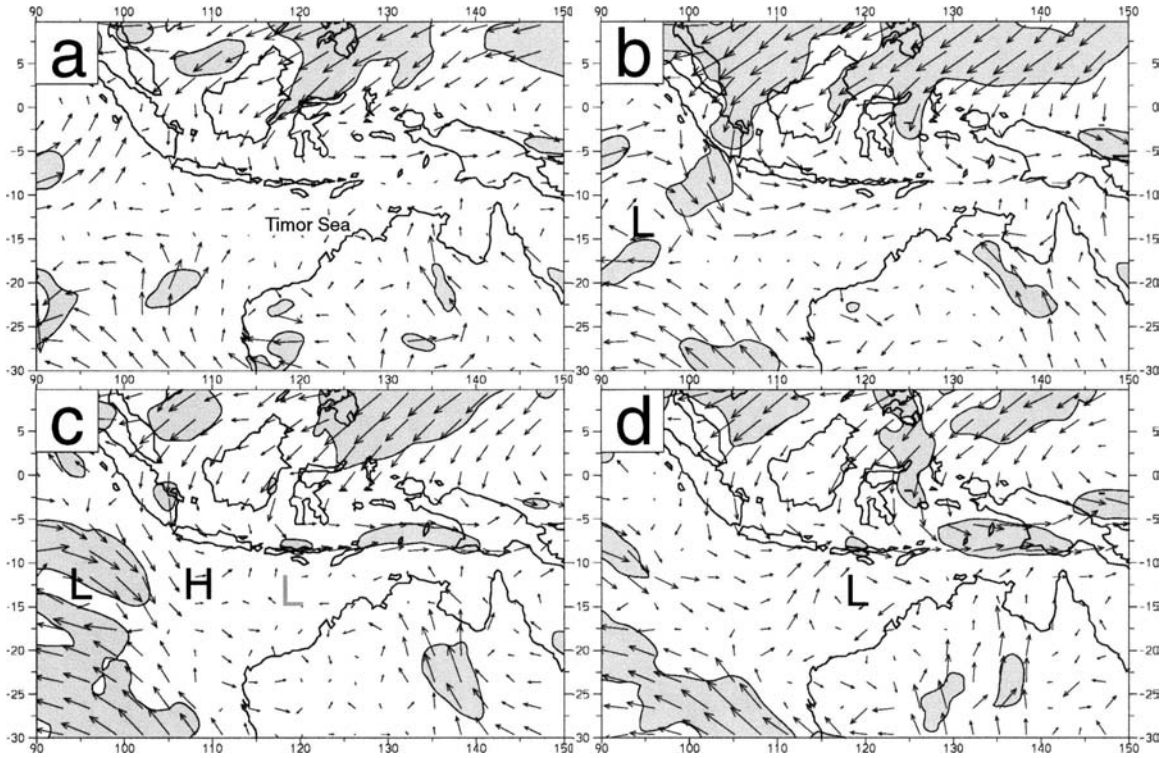

FIG. 2. LAPS375 wind analyses on the 850-hPa surface prior to TC Chris genesis at (a) 1100 UTC 27 Jan, (b) 29 Jan, (c) 31 Jan, and (d) 1 Feb 2002. Shading represents winds greater than 10 m s^{-1}. The cyclonic and anticyclonic circulations discussed in the text are indicated by the letters L and H.

These images show a preference for convection on the western and northern sides of the large-scale low-level circulation (e.g., Figs. 4a–d). They also show periods of enhanced and suppressed convection. Note the reduction in deep convective activity (cold CTT) between Fig. 4f [1300 local daylight time (LDT)] and Fig. 4g (1900 LDT), for example, and the redevelopment of deep convection by 0100 LDT in Fig. 4h. The pattern was repeated also on the following day (not shown). This cycle appears to be diurnal in nature with suppressed deep convection in the afternoon and enhanced deep convection at night, but requires further diagnosis.[1] In addition to the apparent diurnal regulation of convective activity, the structure of the convection changed (on time scales greater than diurnal) from local convective regions, often isolated, moving cyclonically with the background flow (Fig. 4a–f), to larger convective regions near the center of the more organized large-scale cyclonic circulation (Fig. 4h,i).

The scatterometer wind data temporal resolution (12 hourly) is insufficient to identify the primary and secondary vortex enhancement mechanisms. However, combined with the satellite imagery a relationship between convective activity and low-level vortex enhancement can be inferred. There is good evidence of a convective burst, labeled 4 in Fig. 4e, of similar scale[2] to TC-LAPS updrafts examined in Part I, followed by a more organized and focused low-level circulation evident in the next available scatterometer image. Prior to the burst, Fig. 4d shows the large-scale low-level cyclonic wind center was near 14.5°S, 121°E, about 200–250 km south of the convective burst labeled 4 in Fig. 4e. Three hours later the cloud surrounding convective burst 4 had grown significantly in areal extent, with further evidence of very cold CTT embedded (Fig. 4f). Additional satellite images (not shown) suggest deep convection was active in cloud complex 4 for more than 3 but less than 6 h. The identity and location of cloud complex 4 could still be inferred one hour prior to the next available scatterometer image (not shown). Track-

[1] We are not aware of any studies of the diurnal cycle in the TC Chris location, but studies of regions nearby (Keenan et al. 1989) suggest the convective peak should appear between about 0200 and 0900 local time with a lull 12 h later.

[2] The TRMM data suggests the convective region is greater than 50 km in diameter.

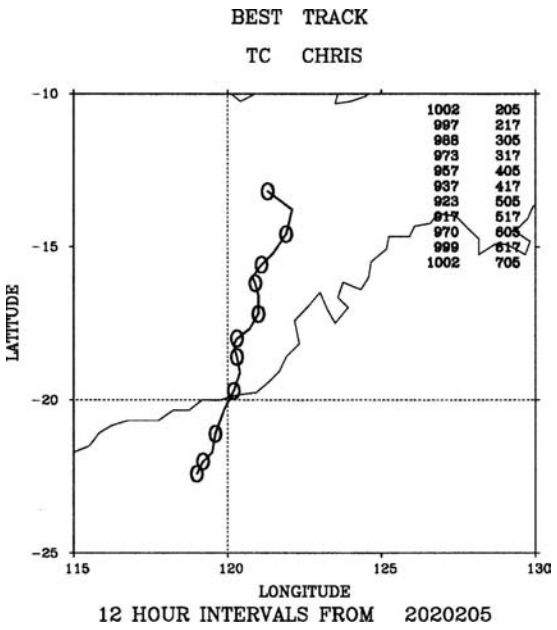

FIG. 3. Map of the TC Chris track after genesis. Estimated central pressures and corresponding date/times are listed in the top right corner of the image.

ing the cloud associated with this convective burst reveals it followed a cyclonic path to a position (arrowed in Fig. 4g) about 100 km northeast of the now considerably more focused low-level circulation center inferred from the wind barbs in Fig. 4g, and about 50 km east of the official storm center location determined by the Western Australian Regional Forecast Office.

The coming together of the large-scale circulation center and the region of intense convection (and the later remnants of intense convection), and the focusing and intensification of the low-level circulation are all consistent with model features presented below. Furthermore, this pattern is consistent (although not conclusive) with the hypothesis that the convective burst with a dominant CDP can act to focus and organize the larger-scale environment.

c. *Verification: Model–satellite comparison*

In the right-hand column of Fig. 4 vertical velocity on the $\sigma = 0.25$ surface and horizontal winds on the $\sigma = 0.9943$ surface are presented over the same domain as the corresponding satellite images in the left column (see Fig. 1 for the position of the domain relative to the entire TC-LAPS domain). The $\sigma = 0.25$ level is used to highlight the more intense updrafts representing deep convection in the model, and the wind vectors on the $\sigma = 0.9943$ surface are included to represent the near-surface winds. This combination was chosen for direct comparison with the satellite and scatterometer winds presented in the left column of Fig. 4. There is a time difference of about 30 min between the satellite and model images. At the initial time (1100 UTC 1 February 2002; Fig. 4a) the location of the modeled deep convection is consistent with the colder cloud tops present in the satellite image, which reflects the influence of the CTT nudging in the dynamic initialization scheme. The low-level circulation has also been well captured by the analysis. In the analysis, the convergence beneath the largest convective region (labeled 1 and B), and the more intense winds on the northern side of the large-scale circulation, have been well represented. The analyzed low-level circulation appears to be more circular than the flow indicated by the scatterometer winds (the latter, possibly an artifact of the scatterometer ambiguity processing). Over the next 24 h (first 24 h of the model simulation; Figs. 4a–g) the development and decay of model-forecast convective regions and observed regions of cold CTT do not remain synchronized or collocated. However, both show a preponderance of convection in the northwest quadrant and to a lesser extent the northern quadrant. This similarity in the broader-scale convective activity suggests the model is capturing large-scale convective forcing. In the next section we suggest this forcing may be associated with the sloping-with-height monsoon low that favors (suppresses) convection on the downtilt (uptilt) side.

Judging by the apparent modeled and observed low-level centers of rotation, the circulation "track error" appears to be increasing by a little more than about 100 km $(12\ \text{h})^{-1}$ (not shown). The modeled circulation center moved to the southwest while the observed center of rotation (scatterometer determined) moved to the southeast. Although this divergence of the modeled and observed trough centers has important implications for the ultimate location of the forecast TC genesis and TC track, it will not be investigated further here since our primary focus is on identifying and illustrating the TC genesis process in TC-LAPS. However, sensitivity studies have shown that the developing TC becomes collocated with the monsoon depression center irrespective of convective locations. Initially this is due to the developing storm/vortex spiraling in toward the monsoon depression center. Then the lowering pressure minimum associated with the developing storm/vortex becomes the monsoon depression center. Thus, both the monsoon depression center and the location of persistent convection appear to be important for determining the position of TC formation. The TC-LAPS sensitivity studies have shown this shift can lead to a difference of about 100 km in storm location after 24 h.

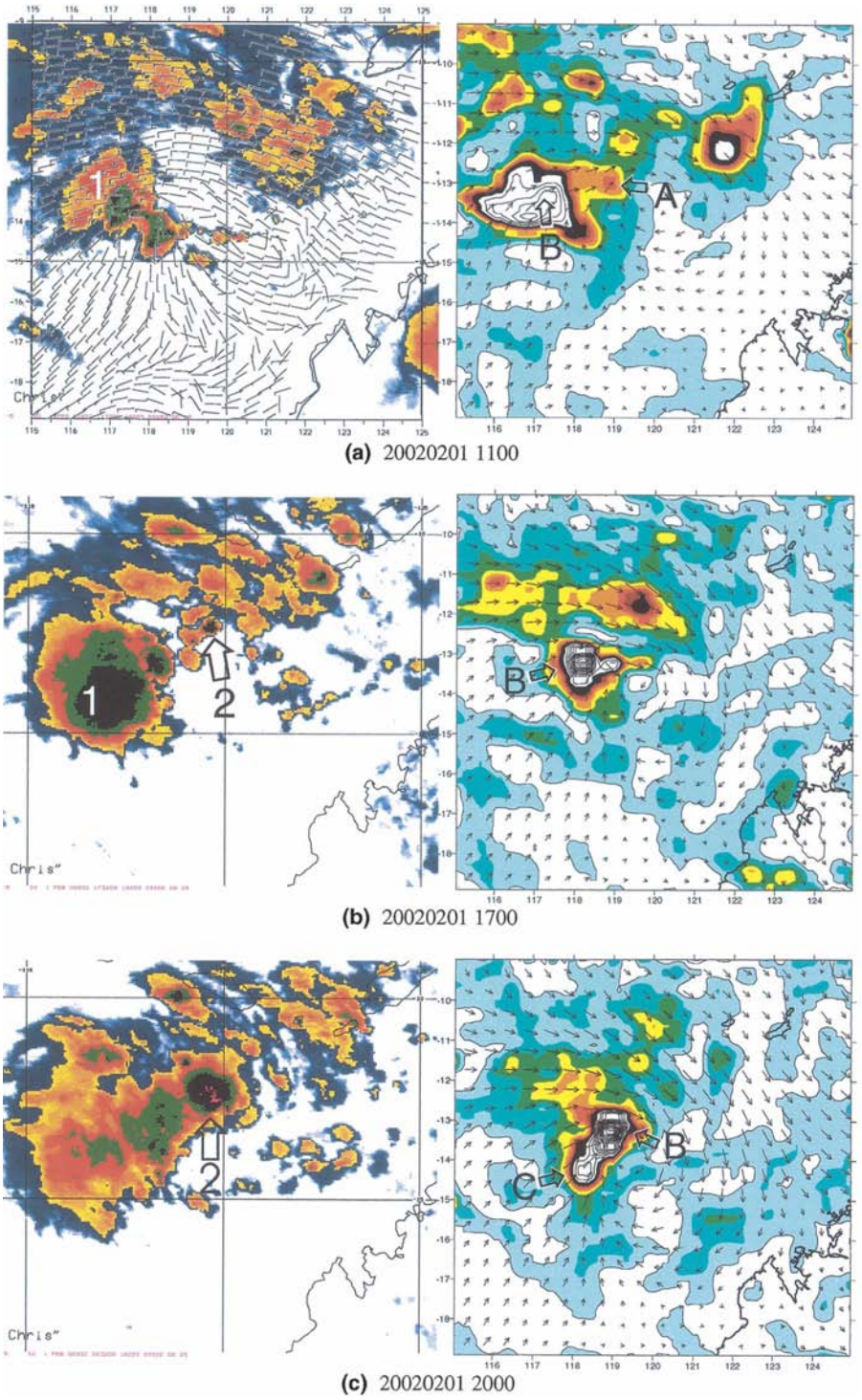

FIG. 4. (left) Satellite images illustrating cloud-top temperatures with scatterometer winds superimposed where available and (right) a representation of the equivalent model structures: vertical motion on the $\sigma = 0.25$ surface and horizontal winds on the $\sigma = 0.9943$ surface. The dates and times of each pair of images are (a) 1100, (b) 1700, (c) 2000, (d) 2300 UTC 1 Feb 2002; (e) 0200, (f) 0500, (g) 1100, (h) 1700, and (i) 2300 UTC 2 Feb 2002. The numbers 1–5 and the letters A–C correspond to particular convective bursts discussed in the text. Model updrafts greater than 2 Pa s^{-1} (~50 cm s^{-1} at 250 hPa) are contoured (interval = 0.5 Pa s^{-1}, ~13 cm s^{-1} at 250 hPa). Vertical and horizontal axis units are degrees latitude and longitude, respectively. Scale bar units are Pa s^{-1} for the model and K for the satellite.

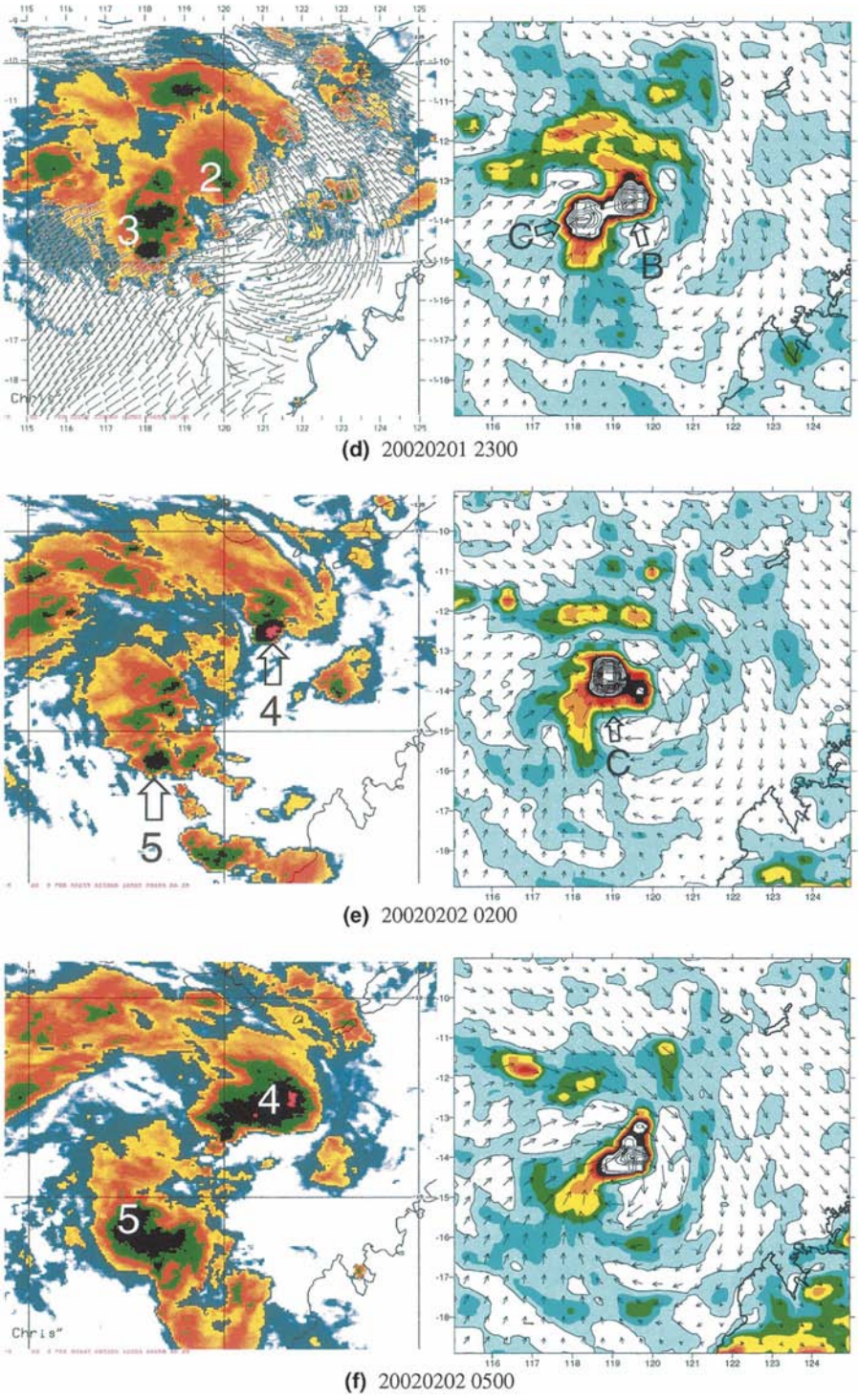

FIG. 4. (*Continued*)

Despite the discrepancy between observed and modeled centers of rotation, the overall structure of the convection/updraft and cloud-free/downdraft regions is quite similar in the first 12 h. After 9 h, for example, Fig. 4c shows a similar orientation of the cloudy/clear-sky regions, represented in the model by the large updraft wind speeds to the northwest and downdraft or weak updrafts to the southeast. The main difference is

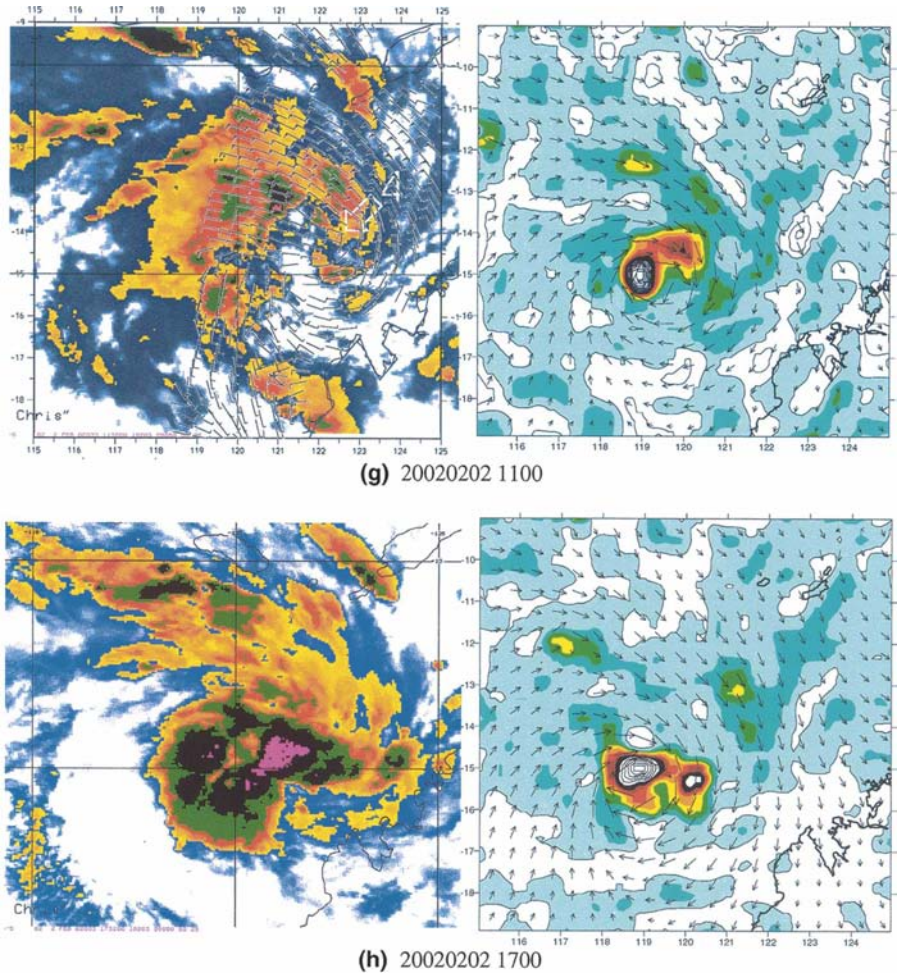

FIG. 4. (*Continued*)

the horizontal scale of these patterns. In the model the scale is smaller and more tightly focused on the center of rotation. This is evident in Fig. 4d. At this time the similarities in structure include a large and intense convective burst to the west of the circulation center (labeled 3 and C), a neighboring convective burst to the northeast (2 and B), and a curved band of convection to the north. The modeled neighboring convective bursts are closer together than those observed, and the modeled band of convection to the north is closer to the two main bursts. This contracted scale in the modeled fields could be due to a more developed large-scale modeled storm than that observed; that is, the genesis process during the first 12 h of the simulation may have been more rapid than that observed.

A factor that might contribute to the more rapid genesis is a tendency for the modeled convective updrafts to be longer-lived and larger than the observed convective regions, during the early stages of genesis. If the net modeled convection is thereby greater than that observed, then the more advanced large-scale spinup by the SSI process may have contributed to this contraction of scale. The longer life of modeled convective updrafts is evident in the sequence of images presented in Figs. 4b–f (3 h apart). During this time we labeled five convective bursts that developed, of which three decayed. Over the same period of time in the model, only two bursts developed (B and C) and only B decayed. Of the many simulations we have run with TC-LAPS, longevity as well as intensity of convection have been important factors that contribute to the primary vortex enhancement mechanism (Part I), and the SSI secondary vortex enhancement mechanism.

The rate of genesis early in the simulation may also be affected by the model's response to the convective parameterization. Ideally each updraft represents an ensemble of convective cells of smaller spatial and possibly smaller temporal scale than the resolved updraft (e.g., Arakawa and Schubert 1974; Tiedke 1989). Such parameterization schemes are designed to redistribute

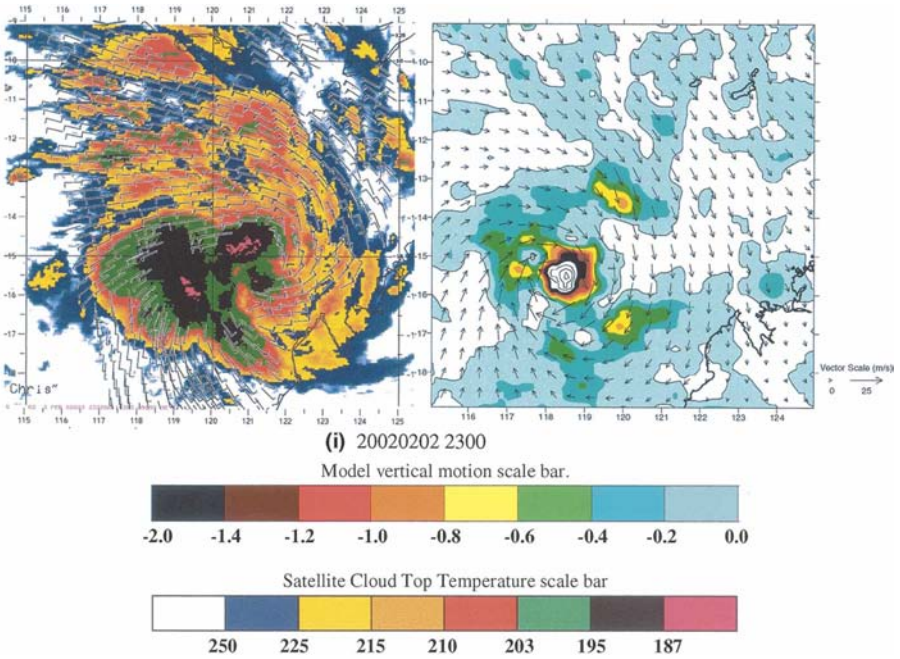

FIG. 4. (*Continued*)

equivalent quantities of heat and moisture to that distributed by the unresolved convective activity. It seems unlikely that the vorticity enhancement in the model updrafts would accurately represent the vortex enhancement by multiple vortex cores in real convective regions. If the modeled updraft focused vorticity and trapped heat energy more efficiently than the true convection it was representing, then both secondary vortex enhancement mechanisms (vortex upscale cascade and SSI) would be expected to proceed more rapidly in the model than the real atmosphere. This may explain some or all of the apparent more rapid intensification of the modeled vortex.

Typically, only one intense convective burst is active at a time in the TC-LAPS simulations (e.g., Part III). Exceptions include a few occasions during the first few hours of a simulation, and in TC Chris when a new convective burst emerged prior to the demise of an existing burst (e.g., B and C in Fig. 4), but these were relatively short lived, lasting only 4–6 h. The forcing of convective scales to a minimum resolvable scale, greater than that observed during the early stages of genesis may inhibit growth of additional nearby updrafts by exhausting CAPE. Although probably unrealistic during the early genesis stages, satellite observations suggest the TC-LAPS pattern may be realistic in the later stages. For example, Fig. 4h shows an area of CTT less than 187 K of about 1° in diameter. The TRMM data (not shown) identifies convective rain rates in fifteen $0.25° \times 0.25°$ square pixels in this region, and a further five pixels that fall within 20% of the 10 mm h^{-1} convective rain-rate threshold. Together they form two side-by-side contiguous convective regions. One or two large MCS-scale bursts were also active in the later genesis stages of TC Oliver (Simpson et al. 1997), Typhoon Robyn (Harr et al. 1996), and Typhoon Irving (Ritchie and Holland 1997). Our estimates of the associated deep convective region scale in these papers are consistent with the TC-LAPS updrafts and Gray's (1998) extreme convection that he notes can act as the "focus from which the centers of tropical cyclones develop". It may be that in the real atmosphere the deep convective scales build with time, particularly if convection is favored in regions of existing/remnant vortices that are growing in scale through the upscale vortex cascade process.

3. TC Genesis in TC-LAPS: TC Chris

In this section we illustrate the development of an intense upright vortex in response to three convective bursts that occur within the first 18 h of the simulation. At this time a warm-cored vortex with a radius of maximum wind of 70 km and maximum mean azimuthal wind speed in excess of 20 m s^{-1}, had developed (not shown), which satisfies the Australian region definition of a tropical cyclone (mean wind speed greater than 17 m s^{-1}). The development process is illustrated in Fig. 5

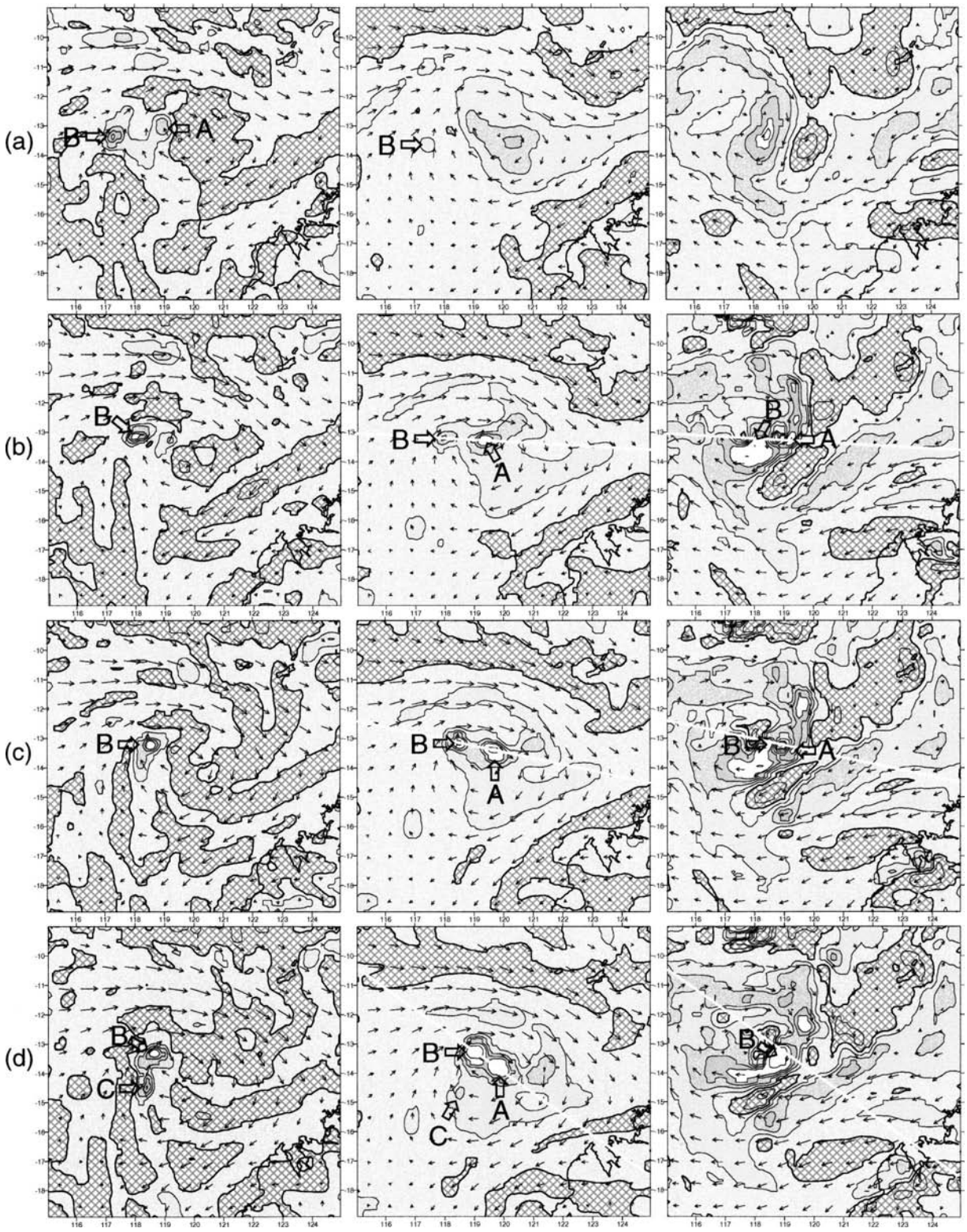

FIG. 5. (left panels) Divergence on the $\sigma = 0.85$ surface with horizontal wind vectors, (center panels) Ertel's PV on the $\sigma = 0.85$ surface with horizontal wind vectors, and (right panels) PV on the $\sigma = 0.5$ surface with horizontal wind vectors, for the simulation of TC Chris initialized at 1100 UTC 1 Feb 2002. The times of the images presented are (a) 1100, (b) 1500, (c) 1700, (d) 1900, (e) 2100, (f) 2300 UTC 1 Feb 2002; (g) 0200 and (h) 0500 UTC 2 Feb 2002. Cross-hatching represents divergence and anticyclonic PV. For contour intervals, multiply scale bar values by 1.0×10^{-4} s^{-1} and 1.0 PVU (1.0×10^{-6} K kg^{-1} m^2 s^{-1}; Hoskins et al. 1985) for divergence and PV, respectively. White lines mark the location of vertical cross sections presented in Fig. 6. Vertical and horizontal axis units are degrees latitude and longitude, respectively.

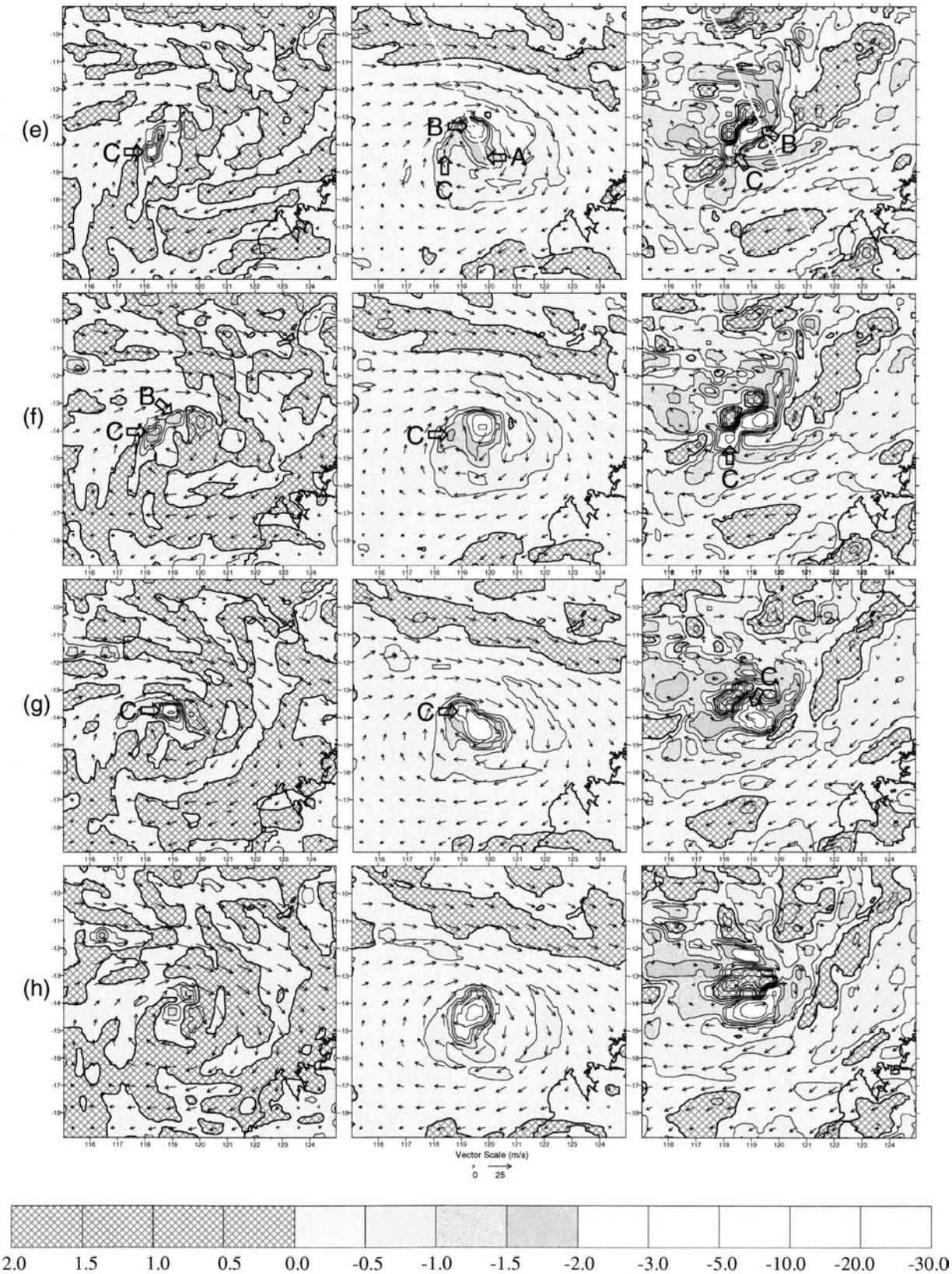

FIG. 5. (*Continued*)

using low-level horizontal convergence (left panels) to identify deep convective regions, and Ertel's potential vorticity (PV) at low and midlevels (center and right panels, respectively) to demonstrate the vortex evolution. Ertel's PV is devined as

$$\mathrm{PV} = \frac{1}{\rho}\boldsymbol{\zeta}_a \cdot \boldsymbol{\nabla}\theta,$$

where ρ is density, $\boldsymbol{\zeta}_a$ is the absolute vorticity vector, $\boldsymbol{\nabla}$ is the 3D gradient operator, and θ is potential temperature (e.g., Hoskins et al. 1985).

At the initial time a large-scale (300–500-km diameter) column of maximum cyclonic PV, associated with the monsoon depression, sloped northwestward with height. Regions of convergence (divergence) on the southwest (northeast) flanks are present at low levels. This is consistent with Jones (1995), in which convergence (divergence) is preferred in the downtilt-left (uptilt-right) quadrant of a dry, initially barotropic tilted vortex in the Southern Hemisphere (where left and right are relative to an observer facing the direction of tilt). Embedded in the general convergent region are two centers of more intense convergence labeled A and B (Fig. 5a). The centers are located about 100 km (A) and 250 km (B) from the center of rotation inferred from the horizontal wind vectors, and even further from the $\sigma = 0.85$ maximum cyclonic PV anomaly. Both centers are associated with the convective bursts labeled A and B in Fig. 4a. [Figure 4a is not representative of the relative convective intensities in the first few hours of the simulation. Within the next hour or so the size and intensity of B decreased and A increased until they were of similar size and intensity (not shown).]

In Part I it was demonstrated that deep intense convective updrafts in an environment of sufficient low-level absolute vorticity resulted in significant enhancement of absolute vorticity on the scale of the updraft because of convergence/stretching and vertical advection. Following the Haynes and McIntyre (1987) representation of the PV tendency in flux form, the corresponding development in PV terms can be explained purely as a horizontal redistribution of PV, involving both advective and nonadvective components. In the appendix we note that horizontal PV convergence/divergence (incorporated in the advective flux) can only lead to local changes in PV magnitude (e.g., PV convergence into updrafts enhances the PV magnitude), whereas local PV changes associated with vertical advection and tilting-like effects in and across updrafts (incorporated in the nonadvective flux) can lead to a local PV source in the updraft with a compensating PV sink at the updraft edge. Thus the PV core development evident in Fig. 5 can be attributed to PV convergence and a vertical advection-like effect in convective updrafts.

a. Low-level PV development, 0–6 h

Growth of PV anomalies in the vicinity of convective bursts is evident throughout the simulation. Within the first four hours PV on the $\sigma = 0.85$ surface increased significantly in the vicinity of both convective bursts (A and B) and the large-scale center of rotation had shifted toward the PV anomaly associated with burst A (Fig. 5b). By this time the convection associated with A had greatly subsided and B had become the dominant convective burst. Despite the longer-lived and sometimes more intense convection associated with B during the first four hours, the PV anomaly associated with A was double the strength of the anomaly associated with B at low levels ($\sigma = 0.85$). This is likely to be due to the differing PV magnitudes in the environments in which the two convective bursts developed; that is, the relative intensities of convergence may have been similar, but the magnitudes of PV substance to be converged differed by about a factor of 2. Persistent convection in burst B continued to intensify PV at low levels, beyond the life of burst A. After 6 h (Fig. 5c) the PV associated with convective burst B, at low levels, was almost as intense as the remnant PV from burst A [>5 potential vorticity units (PVU), where 1 PVU = 1.0×10^{-6} $\mathrm{m^2\,s^{-1}\,K\,kg^{-1}}$] now at the center of the large-scale circulation. Also at this time the PV had been intensifying at mid levels ($\sigma = 0.5$) immediately above the growing low-level PV anomaly.

b. Midlevel PV development, 0–8 h

At the initial time there was little or no vertical coherence in the PV structures between the $\sigma = 0.85$ and $\sigma = 0.5$ surfaces. On the $\sigma = 0.5$ surface (Fig. 5a) a ring of enhanced PV around the large-scale midlevel cyclonic circulation (west of 119.5°E) was present. A band of cyclonic PV extending to the east (associated with cyclonic shear on the northern flank of the easterly wind maximum) was also present. Figure 5a shows anticyclonic PV in between these two cyclonic PV features (near 13°–14°S, 120.0°E). With time the cyclonic PV intensified on the southeast part of the cyclonic PV ring, while the tongue of anticyclonic PV moved to the southwest, which served to further separate the cyclonic PV ring from the PV band to the east (Fig. 5b). In addition to this, anticyclonic PV began to appear in the center of the PV ring (Fig. 5c). The vertical shear, determined from comparisons of the horizontal flow

between the middle and right panels, is consistent with the interpretation that this anticyclonic PV development resulted from the tilting-like effect that compensates the vertical advection-like effect described in the appendix. Kurihara and Tuleya (1981) identified the same positive and negative vortex enhancement relationship between vertical advection and tilting in their convective updrafts.

The midlevel mix of positive and negative PV took considerable time to become organized into a more symmetric PV distribution with a strong cyclonic PV core maximized at the center. The process began when an intense midlevel PV core developed at the location of the convective burst B updraft. The development of this core in absolute vorticity terms was documented in Part I and illustrated in Fig. 3 of Part I. The appearance of this PV core is evident in Figs. 5c,d. Note the small region of enhanced PV (labeled B in Fig. 5c, coincident with the updraft in Fig. 4b) to the north of the main midlevel PV maximum, and the significant enhancement in the nearby location 2 h later (Fig. 5d). The PV appears to have been ingested from the main midlevel PV maximum into the growing PV anomaly associated with convective burst B. In this way PV anomalies with little or no vertical coherence can become organized into an upright PV core.

The PV ingestion adds another level of complexity to the relatively simple dry vortex merger process, in which large and intense vortices dominate (e.g., Wang and Holland 1995). Convergence associated with intense convection in the vicinity of PV anomalies can be considerable in the low to mid levels, and as a consequence nearby PV substance can be ingested and concentrated into a PV anomaly associated with active convection. This scavenging of PV can switch the relative intensities of nearby PV anomalies; that is, weaker anomalies associated with active convection can draw PV from stronger anomalies associated with decayed or decaying convection, and thus reverse the power balance in the vortex interaction. H04 term this process diabatic upscale vortex cascade. In the above case only one convective burst was active (B) and much of the PV substance located to the south and southwest at mid levels (Fig. 5c) would appear to have been ingested into the anomaly associated with burst B (Fig. 5d).

c. Diabatic upscale vortex cascade

The development and interaction of the PV cores associated with bursts A and B, is further illustrated in Fig. 6, which shows vertical cross sections passing through the center of each core at 2-h intervals (the same sections and times were used in Fig. 3 of Part I to illustrate the primary vortex enhancement mechanism). Four hours into the simulation, Fig. 6a shows PV core B is weaker than core A (cf. Fig. 5b). Two hours later, core B had intensified and increased in vertical extent, while core A had weakened considerably at mid levels (Fig. 6b). This midlevel weakening is partly due to shear tilting core A slightly out of vertical alignment (and hence out of the plane of the vertical section). The shear vector across core A between $\sigma = 0.5$ and 0.85 at this time is about 11 m s^{-1} pointing almost directly due west (averaged over a 60-km diameter), which is consistent with the near 0.5° longitude difference in core A locations at these two levels in Fig. 5c. (The large zonal tilt is only slightly out of alignment with the Fig. 6b cross section.) Within another 2 and 4 h (Figs. 6c,d, respectively), core A appears to have merged and become ingested by core B at low levels, with core B intensifying at the cost of core A. Convergence plots on the same vertical sections as Figs. 6b,c (not shown), illustrate extensive areas of horizontal convergence in the vicinity of the updraft, including the left half of the remnant PV core A, and extending to a depth of about 8 km. This suggests the merger of core A into core B, evident in Figs. 5 and 6, is amplified by convergence into the strong updraft of convective burst B, which satisfies our definition of diabatic upscale vortex cascade.

The anticyclonic PV regions on the edges of the vertically growing PV cores in the upper troposphere are also noteworthy. We attribute these to the tilting-like and vertical advection-like effects described in the appendix. It is most evident in Fig. 6c, where the apparent upward growing PV anomaly B is accompanied by an apparent downward growing anticyclonic PV anomaly to the left. This pattern is not evident in Fig. 6d because the cross section does not intersect the main anticyclonic PV anomaly. (Smoothing in Fig. 6d has smeared out a narrow anticyclonic PV anomaly that can be inferred from Fig. 5e at midlevels.)

d. Low-level PV development, 6–18 h

The low-level diabatic merger described above is also evident in Figs. 5c–e. Figures 5e,f show the anomaly associated with burst B also appears to ingest PV from the newly forming anomaly associated with the emerging convective burst C (see Fig. 4).

During this time, hourly images (not shown) illustrate a transition from anomaly B orbiting anomaly A to the remnants of A orbiting B as B became the large-scale circulation center. As B intensified its interaction with A evolved. Initially as a weak PV anomaly, it was advected by the large-scale flow associated with A (Figs. 5b,c). As its intensity became comparable with A the Fujiwhara corotation effect was evident (Fig. 5c,d),

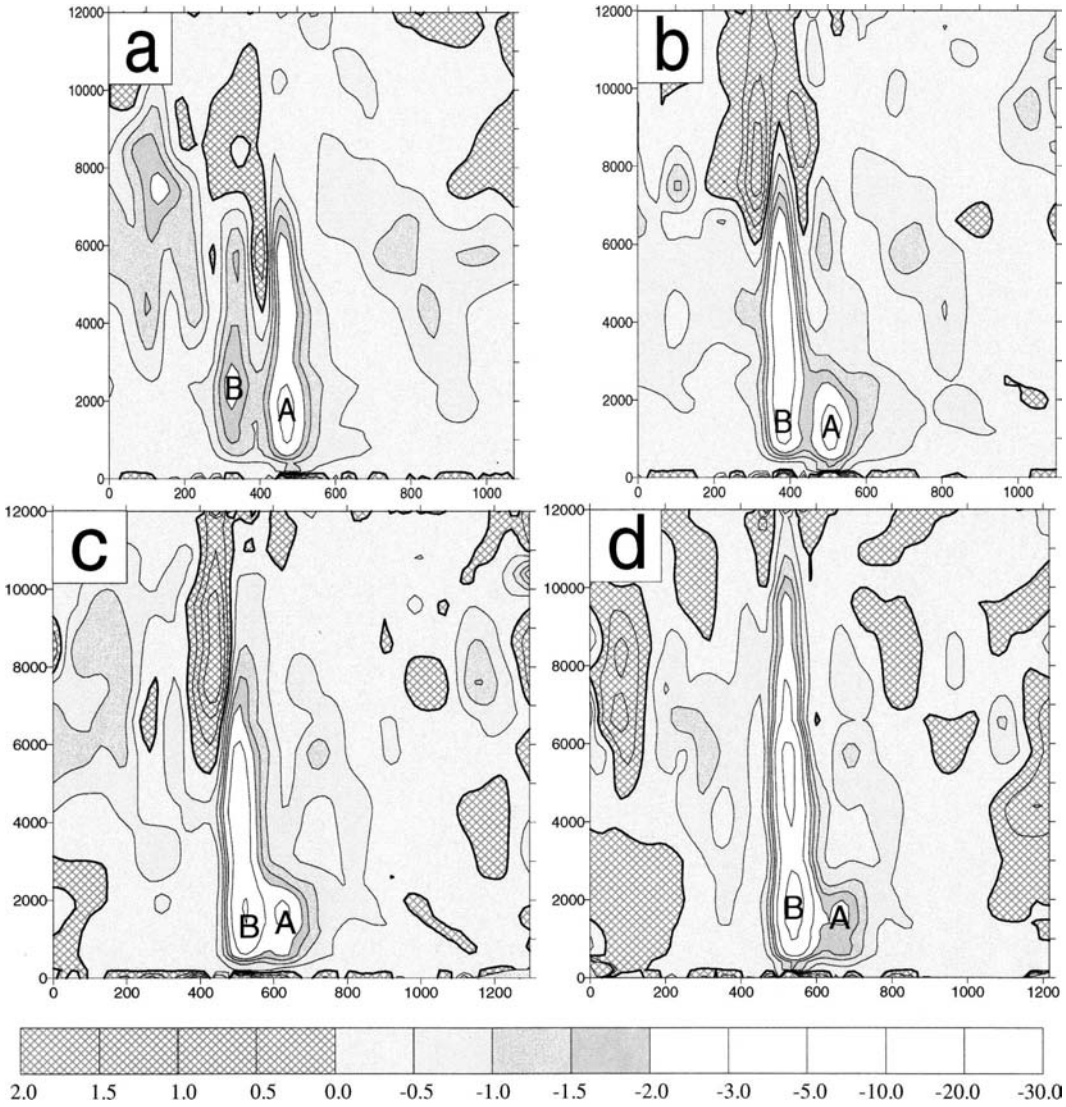

FIG. 6. Potential vorticity on vertical sections passing through the two dominant $\sigma = 0.85$ PVU anomalies at (a) 1500, (b) 1700, (c) 1900, and (d) 2100 UTC (same times as Figs. 5b,c,d,e). Vertical and horizontal axis units are m and km, respectively. Images (a) and (b) run nearly east–west, whereas images (c) and (d) run approximately northwest–southeast; hence the horizontal scales of the latter two are larger than the former two. The scale bar is identical to Fig. 5 (units are PVU). The locations of each cross section are marked by white lines in Fig. 5. The vertical and horizontal axis units are m and km, respectively.

although only briefly since B soon became significantly more intense than A (Fig. 5d) and A was ingested, sheared, and axisymmetrized by B (Figs. 5e–f).

The sporadic nature of the alternating convective bursts labeled A, B, and C in Figs. 4a–e, responsible for the vortex interactions described above, is reminiscent of the pulsing growth and decay of convective bursts evident in the satellite images (section 3b). The direct effect of the alternating bursts of convection in the low-level PV structure is also evident in Figs. 5e–g (these figures correspond to the same time period represented in Figs. 4c–e). The small PV anomaly labeled C, in Fig. 5e rotated cyclonically about the main vortex center and intensified (Fig. 5f). Within the next three hours it approached the intensity of the central PV anomaly (Fig. 5g). At this time updraft B had long since subsided (Fig. 4e), and updraft C was beginning to weaken during a widespread convective lull period (Fig. 4f). Hourly images during this time (not shown) illustrate the merger of anomaly C with the central anomaly resembled adiabatic merger in which vortex advection effects dominated, unlike the convectively active

phases when vortex dominance and growth was determined by convective intensity (diabatic upscale vortex cascade).

One peculiarity of the TC Chris simulation not observed in other simulations we have examined in detail (Part III) is the semipredictable nature of the convection, due to the preferred convergence area brought about by the tilted monsoon depression (introduced above).[3] In this simulation and in a sensitivity simulation of TC Chris, convective bursts born in a preferred convergence zone were advected cyclonically with the background flow and decayed soon after leaving the preferred convergence zone. An example of this is evident in the left panels of Fig. 5. The first burst to be born in the preferred convergence zone was burst B (Fig. 5a). Six hours later (Fig. 5c) the most intense region of convection (B) had rotated to the northwest of the circulation center and inwards. At the same time an elongated region of enhanced convergence extended southward of B, and southwest of the center of rotation (Fig. 5c). Within another two hours (Fig. 5d) a distinct center of convergence had formed to the southwest, coincident with the position of the developing burst C. As burst B was advected to the north of the center of rotation (outside the preferred convergence zone) the associated low-level convergence weakened (Fig. 5f) coinciding with the beginning of the decay of burst B.

e. Midlevel PV development, 10–18 h

Between 10 and 18 h the midlevel PV evolution, like the evolution at low levels, was dominated by convective bursts B and C. One hour earlier (9 h into the simulation) when burst C was beginning to approach burst B in intensity (Fig. 4c), the midlevel PV distribution in the vicinity of burst C was considerably greater than at low levels (about 2 and 1 PVU respectively, not shown). At 10 and 12 h, Figs. 5e,f show this imbalance had grown further (maximum PV associated with burst C at mid levels in excess of 3 PVU). Hourly images (not shown) suggest this growth pattern is due to burst C moving northward (between 8 and 10 h, see Figs. 5d,e) until it intersected the midlevel exhaust plume of elevated PV advected out of the southwest corner of anomaly B (evident in Fig. 5d). It would appear the PV exhaust plume provided a significant midlevel PV source to be concentrated (converged) by the burst C updraft. Thus the midlevel PV anomaly intensified more rapidly because there was more PV substance to be converged than at lower levels.

Alignment of the low- and midlevel PV anomalies continued in the vicinity of the burst C updraft (Fig. 5g), and the beginnings of an upright PV monolith had developed 3 h later (Fig. 5h). The large area of anticyclonic PV to the north of the midlevel cyclonic core in Fig. 5h, gives the impression of a PV dipole. However, the magnitude of the cyclonic anomaly is about 5 times greater than the anticyclonic anomaly. Within another 6 h, the anticyclonic anomaly had weakened considerably and the remnants were ejected through a weak point of the surrounding cyclonic PV ring that opened up to the southeast (not shown). Throughout that time the cyclonic anomaly strengthened on the whole, increased in size, and became more symmetric, mirroring the development at lower levels.

f. Summary of PV phenomenology

The details of the PV interactions illustrated in the previous subsections describe a complex interaction between PV anomalies that develop in convective updraft regions. The transitory nature of the convective bursts adds further complexity to the process. Despite the apparent disorganization, the intrinsic tendency toward horizontal axisymmetrization and vertical alignment persists in the construction of an upright PV monolith that ultimately forms the TC. We believe the following points regarding the PV interactions are of physical interest because they either are, or may well be, active in the real genesis environment.

1) The growth of PV cores associated with convergence and the vertical advection effect in active convective regions.
2) The PV convergence into convective regions focuses disorganized PV anomalies into a central core, thereby aligning low- and midlevel PV structures.
3) Deep convective bursts leave behind remnant PV cores that outlive the convection.
4) Deep convective bursts converge into their updraft cores all available PV, including remnant PV cores, so the magnitude and size of the dominant PV core increases with each successive burst, provided new bursts develop sufficiently close to the remnant PV core.
5) Vortex–vortex interactions between PV cores are complicated by rapidly changing intensities. An initially weak but intensifying PV core associated with a young convective burst will at first be dominated by other more intense nearby PV cores. But as the relative intensities change, the dominance balance will be reversed, particularly if the active burst is ingesting PV from the nearby PV core.
6) An intensifying PV core tends to intensify at varying

[3] We have also observed what appears to be a preferred convergence region to the west of the main large-scale cyclonic circulation in satellite imagery of TC Oliver (Coral Sea 1993).

rates with height, depending on the vertical distribution of PV in the vicinity of the updraft core and the magnitude of the convergence.

7) Shear tends to tilt and weaken PV cores, whereas active convection vertically aligns and intensifies the cores. Variations in convective intensity in a sheared environment can lead to a cycle of weakening and tilting, then intensification and alignment.

The above points are found to be valid for all TCLAPS simulations we have investigated (e.g., see Part III). Although subtle and not so subtle differences occur between simulations, the fundamental processes of PV core construction in active convective regions and the interaction of PV anomalies to build larger more intense cores prevail.

4. System-scale budgets of tangential momentum and potential temperature

During the first 18 h of the simulation the northwestward sloping with height, large-scale (about 500 km) cyclonic circulation associated with the monsoon depression (Fig. 5a) evolved into a stronger, more vertically aligned large-scale circulation with an upright intense inner core (PV monolith) about 100 km in diameter (Fig. 5h). As shown in the previous section the diabatic upscale vortex cascade can explain much of this PV monolith development. However, the SSI process is not so apparent in Fig. 5, except maybe at radii of hundreds of km (cf. Figs. 5a,h). In this section contributions to the azimuthal mean vortex intensification are investigated using traditional Eulerian azimuthal mean tangential momentum and potential temperature budget equations following H04 and M06. The use of such analyses helps identify which vortex enhancement processes are active, when and where they are active, and the relative contribution of each process to dynamical and thermodynamical changes to the developing azimuthal mean cyclone.

The budget equations used in this paper are identical to those described in M06, except they are centered on the 850-hPa PV centroid,[4] and contributions at hourly intervals are included in the time integration. The motion of the PV centroid is subtracted from the horizontal velocities used in the budget calculations to produce a system-relative budget. In a locally cylindrical coordinate system centered on the PV centroid the azimuthal mean tangential momentum tendency is given by

$$\frac{\partial \bar{v}}{\partial t} = -\overline{u\eta} - \overline{u'\zeta'} - \bar{w}\frac{\partial \bar{v}}{\partial z} - \overline{w'\frac{\partial v'}{\partial z}} + \bar{F}_{\mathrm{sg}}, \qquad (1)$$

MRAV ERRV MVTM EVTM

and the azimuthal mean potential temperature tendency is given by

$$\frac{\partial \bar{\theta}}{\partial t} = -\bar{u}\frac{\partial \bar{\theta}}{\partial r} - \overline{u'\frac{\partial \theta'}{\partial r}} - \bar{w}\frac{\partial \bar{\theta}}{\partial z} - \overline{w'\frac{\partial \theta'}{\partial z}} + \bar{\dot{\theta}}. \qquad (2)$$

MRPT ERPT MVPT EVPT THDOT

The overbars denote azimuthal averages and the dashes denote perturbations from the azimuthal average. The velocity vector components, u, v, and w represent the centroid-relative radial, tangential, and vertical velocities, respectively; θ is potential temperature and $\dot{\theta}$ is the diabatic heating rate. The vertical components of the absolute and relative vorticities are represented by η and ζ, respectively, and r, z, and t represent radius, height, and time.

Following the terminology of M06, the terms on the right-hand side of Eq. (1) are the mean radial flux of absolute mean vertical vorticity (MRAV), the eddy radial flux of eddy relative vorticity (ERRV), the mean vertical flux of mean tangential momentum (MVTM), the eddy vertical flux of eddy vertical momentum (EVTM), and the mean subgrid-scale tendency of tangential momentum, respectively. The latter term is calculated as a residual; that is, the actual change in the azimuthal mean tangential momentum minus the sum of the other four tendency terms. Similarly for Eq. (2), the terms on the right-hand side are the mean radial advection of mean potential temperature (MRPT), the eddy radial advection of eddy potential temperature (ERPT), the mean vertical advection of mean potential temperature (MVPT), the eddy vertical advection of eddy potential temperature (EVPT), and the diabatic heating rate (THDOT).

Each tendency term, integrated over the first 18 h of the simulation, is presented in Fig. 7 [Eq. (1)] and Fig. 8 [Eq. (2)], along with the actual change in the azimuthal mean quantities (except in Fig. 8, where the MVPT term has been replaced with the sum of MVPT and THDOT). A first glance reveals that in general positive contributions from the mean terms (MRAV, MVTM; Figs. 7a,c, respectively) extend to larger radii than the eddy terms (ERRV, EVTM; Figs. 7b,d, respectively). The positive areas of the eddy terms are con-

[4] The PV centroid is calculated over a 3° × 3° box centered on the 850-hPa geopotential minimum, in which the geopotential field has been smoothed using a Barnes analysis with an e-folding radius of 90 km. The positions of the PV centroids have been smoothed in time to remove artificial accelerations due to centers being confined to discrete grid points, and any other small errors associated with the calculation of the PV centroid.

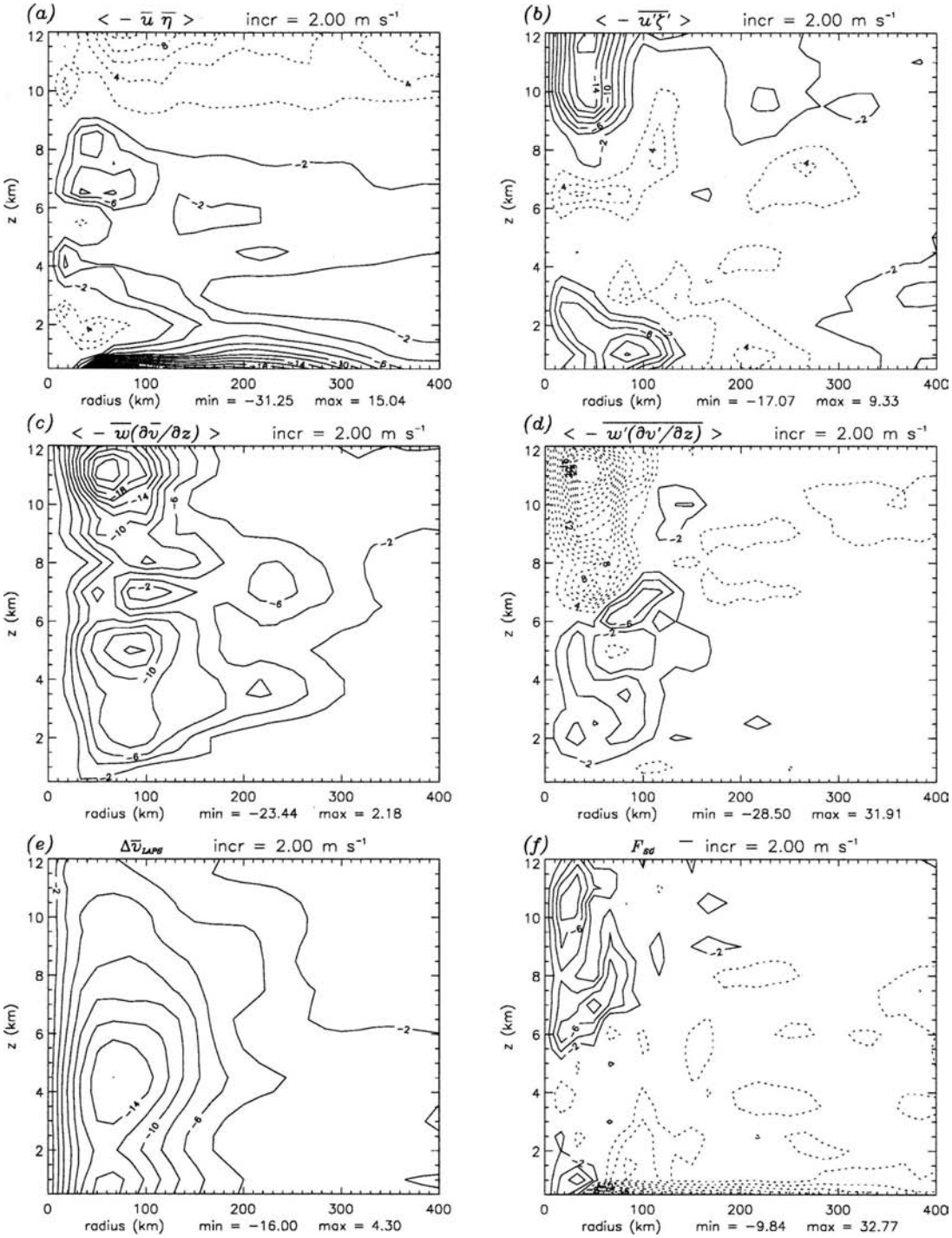

FIG. 7. Time-integrated tendency terms (denoted by ⟨⟩) over the first 18 h of the TC-LAPS TC Chris simulation from the tangential momentum equation [Eq. (1)]. The time integral of (a) mean radial flux of absolute vertical vorticity (⟨MRAV⟩); (b) eddy radial flux of eddy relative vertical vorticity (⟨ERRV⟩); (c) mean vertical flux of mean tangential momentum (⟨MVTM⟩); and (d) eddy vertical flux of eddy vertical momentum (⟨EVTM⟩). The change in mean tangential velocity over the 18 h simulation, $\Delta\overline{v}_{\mathrm{LAPS}}$, is shown in (e), and the difference between the term shown in (e) and all other terms (residual), is shown in (f). Subgrid-scale processes appear in (f). Negative contours (cyclonic in the Southern Hemisphere) are represented by full lines, positive contours represented by dashed lines, and zero contours have been omitted.

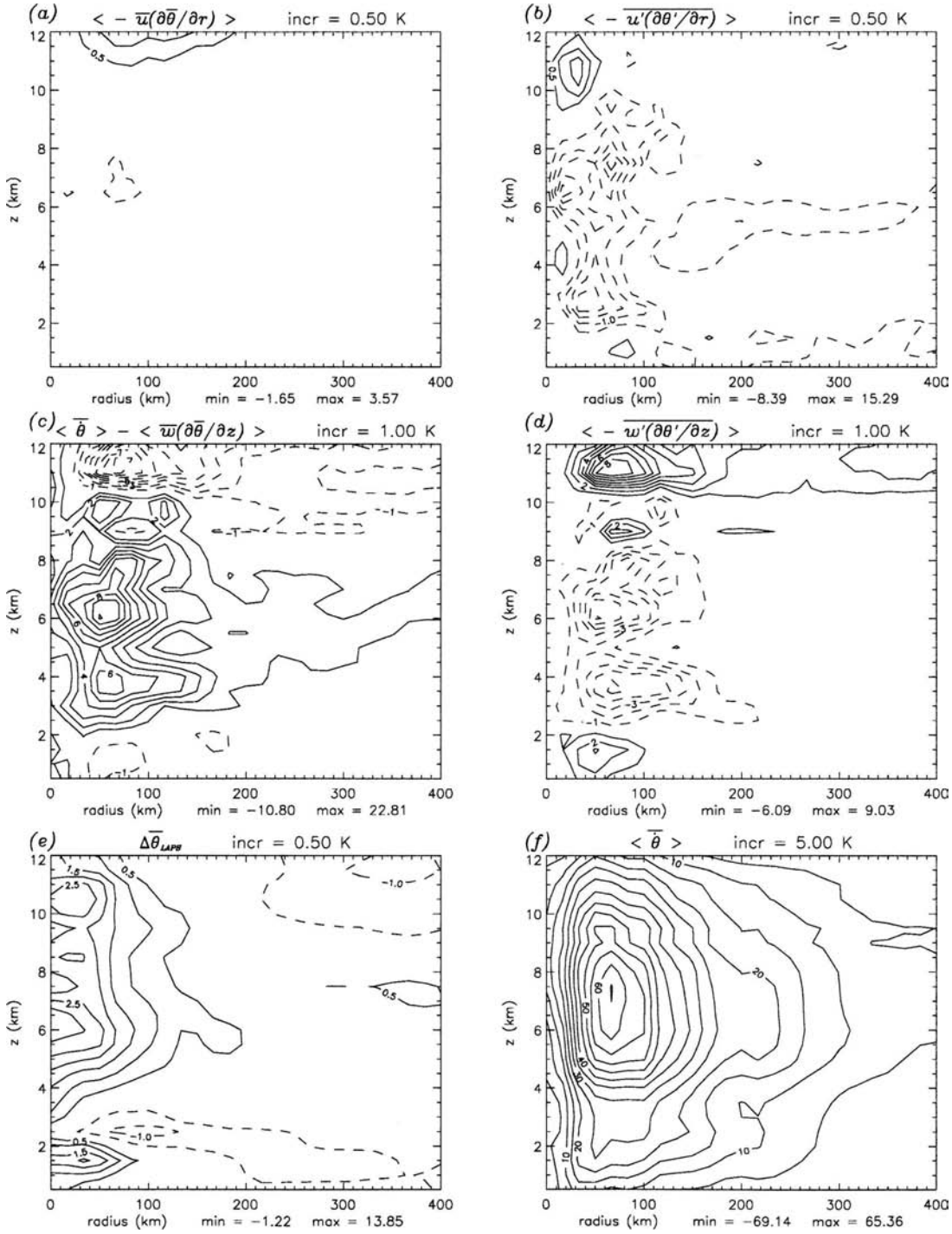

FIG. 8. Time-integrated tendency terms (denoted by $\langle\rangle$) over the first 18 h of the TC-LAPS TC Chris simulation from the potential temperature equation [Eq. (2)]. The time integral of (a) mean radial advection of mean potential temperature ($\langle$MRPT$\rangle$); (b) eddy radial advection of eddy potential temperature ($\langle$ERPT$\rangle$); (c) the mean vertical advection of eddy potential temperature plus the diabatic heating rate ($\langle$MVPT$\rangle$ + $\langle\dot{\theta}\rangle$); and (d) the eddy vertical advection of eddy potential temperature ($\langle$EVPT$\rangle$). The change in mean potential temperature over the 18 h simulation, $\Delta\bar{\theta}_{\mathrm{LAPS}}$, is shown in (e) and the time integral of the mean diabatic heating rate is shown in (f). Note the differences in contour interval. Negative contours dashed and zero contours have been omitted.

fined largely to the lower half of the troposphere and within a radius of 150 km. The positive areas of the mean terms extend beyond 400 km and throughout most of the troposphere, although the greatest positive contributions tend to be confined within the inner 120 km. These figures help illustrate the relative roles the various vortex enhancement processes (primary and secondary) play in spinning up the mean vortex.

a. Direct spinup: Primary vortex enhancement mechanism

The mean terms essentially represent the mean convergence of mean absolute vorticity (MRAV) and the mean vertical advection of mean angular momentum (MVTM). In Part I we showed the primary vortex enhancement mechanism at low to mid levels could be attributed to the convergence/stretching and vertical advection of absolute vorticity, in the model convective updrafts. These model updrafts were largely confined to within 120 km of the PV centroid (not shown), which coincides with regions of significant positive contributions from the horizontal and vertical mean terms (MRAV and MVTM) in Fig. 7. This suggests that the model convective bursts contributed directly to the spinup of the mean vortex. Furthermore, the particularly strong mean vertical term (MVTM; Fig. 7c) reinforces the important role, established in Part I, of vertical vorticity advection throughout the troposphere. For this term to contribute to strengthening cyclonic vorticity in the vicinity of the model updraft, $(\partial\bar{v}/\partial z)$ must be positive (negative) in the Southern (Northern) Hemisphere (cyclonic vorticity decreases with height), thus cyclonic momentum is advected upward throughout the troposphere.

b. Indirect spinup: Secondary vortex enhancement mechanisms

1) SYSTEM-SCALE INTENSIFICATION

The conclusion of H04 and M06 that their system-scale vortex evolution proceeded in near-thermal wind balance is very likely to be valid in the TC-LAPS simulations also. However, we expect it would be more difficult to illustrate in the TC-LAPS simulations because of a combination of relatively coarse resolution and not particularly meaningful or accurate heating rates from the cumulus parameterization scheme at scales of a few Δx (Y. Kurihara 2003, personal communication). These issues could lead to factor of 2 discrepancies between the model-derived and inferred balanced vertical velocities (see, e.g., Möller and Shapiro 2002; cf. Persing and Montgomery 2003; M06). If we assume the mean vortex evolution evolved in near-thermal wind balance then the positive contributions to the mean terms at large radii evident in Figs. 7a,c are likely to represent vortex intensification from the SSI process. (It would be expected that this process would also contribute to mean vortex intensification inside 120 km, although it would be masked by the strong contribution from the direct spinup mechanism.) This result, like that found in H04 and M06, suggests intense convection indirectly intensified the system-scale mean vortex at radii extending beyond the convection, through the enhancement of the system-scale secondary circulation in response to convective heating. Large-radii vortex intensification is evident when the horizontal winds of Fig. 5a are compared with Fig. 5h.

2) VORTEX UPSCALE CASCADE

In general, positive contributions from the eddy terms (ERRV, EVTM) are associated with ingestion/merger and vortex axisymmetrization/strengthening (e.g., Melander et al. 1988; Montgomery and Brunet 2002); these are the processes that contribute to the upscale vortex cascade (H04; M06). As mentioned above the positive eddy contributions were mostly confined to a 150-km radius and roughly the lower half of the troposphere (Figs. 7b,d), which is consistent with the interactions of PV anomalies, associated with the model convective updrafts A, B, and C described in the previous section. The horizontal eddy term is particularly strong inside 150 km, below about 3–4 km (Fig. 7b) and is associated with the horizontal capture of relative vorticity by eddy processes; that is, the merger, ingestion, and axisymmetrization of vortices into the monolithic PV core. Immediately above this positive region, between about 4 and 8 km (midlevels) the horizontal eddy term (ERRV) contributes mostly to a spindown of the mean vortex, particularly between 6 and 8 km. Budget equations integrated over 6-hourly intervals reveal that this negative contribution occurred mostly between 12 and 18 h, and to a lesser extent 6 and 12 h. It appears to be associated with a tilting tendency in an increasing shear environment. The shear magnitude between 1500 and 5000 m (averaged over a horizontal radius of 250 km, not shown) steadily increased from about 5 to 9 m s^{-1} between 6 and 18 h, and decreased at a similar rate after that. Figure 5h shows that the PV monolith did remain upright throughout this period, which suggests a battle between the destructive effects of large-scale shear tilting the PV monolith and the regenerative effects of vorticity enhancement in the updraft cores (evident in the vertical mean term, MVTM; Fig. 7c) may have been in effect.

The strong contribution to cyclonic intensification

above 10 km from the mean vertical term (Fig. 7c) is a reflection of the strong vertical gradients in mean tangential velocity above 10 km (at the top of the large-scale vortex core). The strong negative tendencies in the vertical eddy term (Fig. 7d) are related to the off-center individual model vortex cores. On average these cores were centered on a radius of about 100 km. Outside (inside) this radius the flow within the vortex cores would be faster (slower) relative to the mean background rotational flow, hence v' is cyclonic (anticyclonic) outside (inside) 100 km, and the vertical gradients can be determined from the knowledge that the cyclonic momentum decreases with height at this level. Thus inside (outside) the updrafts $\partial v'/\partial z$ is negative (positive) inside 100 km and w' is positive (negative), which yields positive EVTM (anticyclonic tendency, Southern Hemisphere).

c. Potential temperature budget

The potential temperature budget terms integrated over the first 18 h of the simulation are presented in Fig. 8. The change in potential temperature during this time was greater than 2 K between 4.5 and 11 km in height, inside a radius of about 60 km (Fig. 8e). A low-level heating maximum was present at 1.5 km, with maximum value of about 2 K. The layer of cooling between about 2 and 3 km occurred during the first 6 h of the simulation, and was associated with the horizontal transport of an initial hot spot of about 250–300-km diameter on the eastern flank of the large-scale cyclonic circulation, away from the budget center. The magnitude of this cooling was about 2 K. After the low-level hot spot moved out of the averaging domain the warming was near-uniform above 1 km, within a radius of about 60 km (about 2 K). This in conjunction with the early cooling between 2 and 3 km explains the 0–18-h heating pattern in Fig. 8e.

Figure 8a shows a negligible contribution to heating from the mean horizontal term throughout most of the domain. Between 2 and 10 km, the heating can be explained largely by the excess in diabatic heating compared with the mean adiabatic cooling (Fig. 8c). This excess is relatively small when compared with the actual magnitudes of the mean adiabatic cooling term (not shown) and diabatic heating term (Fig. 8f, note the difference in contour intervals). The near balance of diabatic heating and adiabatic cooling slightly in favor of diabatic heating is also observed in the budgets of Kurihara and Tuleya (1981), H04, and M06. The horizontal and vertical eddy terms provide additional cooling. Convergence of cooler air into the updrafts is a likely explanation for the horizontal eddy term (Fig. 8b).

The significant positive increase in heating below 2 km inside a radius of 100 km (Fig. 8e) is mostly due to the vertical eddy term (Fig. 8d). The heating occurred mostly between 12 and 18 h, when warming in the subsidence region, centered on 2-km elevation, resulted in reduced (increased) static stability above (below) 2 km. In the subsidence region $w' < 0$, and from the above argument, $\partial\theta'/\partial z > 0$ below 2 km (inside a 100-km radius), which explains the positive contribution evident in Fig. 8d.

In summary, the tangential momentum budget has confirmed the importance of both secondary vortex enhancement mechanisms, vortex upscale cascade and SSI; the potential temperature budget has shown diabatic heating slightly in excess of adiabatic cooling was largely responsible for the warm core development, further confirming the importance of the SSI process.

5. Summary and conclusions

In the TC-LAPS simulation of TC Chris a monsoon low tilted to the northwest seemed to contribute to a preferred convergence zone to the west of the low-level monsoon low circulation center (consistent with Jones 1995). The intense convective updrafts tended to form in the preferred convergence zone and weakened as they were advected out of the zone by the monsoon circulation. Drawing from the results of Part I, H04, and M06, we propose that each TC-LAPS convective updraft generated a locally intense cyclonic PV core that ingested/merged with surrounding cyclonic PV anomalies, including remnant PV cores associated with previous convective bursts, thus contributing to local vortex intensification through the diabatic upscale vortex cascade process. The scavenging of cyclonic PV by convective bursts ensured the cyclonic PV cores intensified with each successive convective burst, which ultimately led to the construction of a single upright monolithic cyclonic PV core, about which the TC developed. In addition, we believe the SSI process played an important role in spinning up the TC-LAPS, TC Chris vortex, particularly at large radii.

The diabatic upscale vortex cascade and SSI processes became centered on the PV monolith, thus reinforcing vortex growth on the system scale about a single upright axis. This vortex development pattern is also evident in additional TC-LAPS simulations presented in Part III.

In this first round of investigations into TC genesis in TC-LAPS we have focused on the genesis mechanisms present in the model rather than the forecast accuracy. The first test of any TC-genesis model is its qualitative performance (Does it accurately forecast both forma-

tion and nonformation?), rather than the more quantitative results of formation timing, track, and intensity. Model verification was included to provide some insight into the qualitative performance, despite the main focus of this work being on qualitative results. The deep convection and low-level winds generally compared well with the cloud imagery and scatterometer winds during the early formation stage, although the simulated development occurred more rapidly than that observed.

The horizontal grid spacing confines the simulated convective regions to scales of at least the minimum resolvable scale of about 60 km. Thus the greater rate of development may have been due to convection forced on the minimum resolvable scale early in the simulation, at a time when the satellite imagery suggests multiple shorter-lived and presumably smaller-scale convective regions may have been active in reality. However, an intense convective burst on the scale of Gray's (1998) extreme convection and of similar scale to the TC-LAPS convection was evident in the satellite imagery at a time equivalent to 15 h into the simulation. This shows convective regions of similar scale to the resolved bursts in TC-LAPS may be realistic during later formation stages. The change in the low-level flow pattern indicated by scatterometer wind observations before and after the convective burst suggests it played a role in the enhancement and focusing of the low-level cyclonic circulation; a result consistent with the vortex response to intense convection in the simulations.

Another factor that may result in more rapid genesis in TC-LAPS is the vortex response to the individual updraft core. The modeled convective updrafts develop largely in response to the redistribution of moisture and heat by the convective parameterization scheme. Even if this redistribution accurately represents the transfer of heat and moisture by subgrid-scale convection, it is unlikely that the model-generated vortex core would accurately represent the subgrid-scale vortex cores associated with the subgrid-scale convection, particularly with regard to the efficiency of trapping and converting heat energy to rotational energy.

If the TC-LAPS convection does favor more rapid formation in the early stages of TC genesis, then it might be expected that TC-LAPS forecasts would have a high rate of false alarms. From the simulations we have studied in detail (e.g., see Part III) it would appear the main factors that determine formation or nonformation are the larger scale, net convection, cyclonic environment, and shear intensity. There may be some combination of these variables that defines the limit between formation and nonformation, in which case it will only be when the atmosphere is near this limit that TC-LAPS performance will be challenged. If it were possible to identify the borderline cases, we may indeed find TC-LAPS is biased toward formation in these cases. However, there could be other factors in TC-LAPS that oppose such biases. (A TC-LAPS genesis climatology is currently underway. Despite a tendency for a more rapid genesis rate than observed, we have detected relatively few false alarms.)

Although the observations presented here support the hypothesis that the genesis processes identified in the TC Chris simulation may be active in the real atmosphere, they are not conclusive. Observational data collection at unprecedented spatial and temporal resolution would be required before the theory could be proved or disproved. In the absence of such data the next best tool for investigating TC genesis is a realistic forecast model such as TC-LAPS.[5] The unique initialization procedure used in TC-LAPS ensures initial deep convection develops in locations where it has been observed. Given the critical role deep convection is very likely to play in TC genesis, this initialization procedure is an important component of the system that contributes to the model realism.

Acknowledgments. This work was supported in part by NICOP-ONR Grant N00014-02-1-0431 as part of a collaboration with the Naval Research Laboratory. Additional support came from Grants ONR N00014-02-1-0474, NSF ATM-0101781, and NSF ATM-0132006. Recent support from an ONRIFO VSP Grant N00014-04-1-4062 funded a visit by the lead author to the United States, during which significant advancements in this work were made. We thank Drs. Peter May and John McBride for helpful comments and suggestions, and we would like to acknowledge Dr. Greg Holland for some interesting and illuminating discussions on the topic of TC genesis. Last, we would like to acknowledge the anonymous reviewers, whose suggestions led to improvements in the paper structure and focus.

APPENDIX

Interpretation of PV Tendencies

Haynes and McIntyre (1987, hereafter HM87) expressed the PV tendency equation in flux form. The

[5] A nonhydrostatic NWP system will be available soon, and a state-of-the-art cloud microphysics package has recently been completed (Dare 2004). In the future we plan to repeat the TC genesis experiments at cloud-resolving scales to further investigate the realism of the results presented in this work.

flux measures the rate at which PV substance (PVS) "moves" from one location to another, and the divergence of this flux then describes local changes in PVS. In isentropic coordinates PVS is the component of absolute vorticity normal to the isentropic surfaces. Ignoring friction, the PVS flux vector **J** is represented by

$$\mathbf{J} = (u, v, 0)\sigma Q + \left(\dot{\theta}\frac{\partial v}{\partial \theta}, -\dot{\theta}\frac{\partial u}{\partial \theta}, 0\right). \quad \text{(A1)}$$

Here u and v are the horizontal wind components, σ is the isentropic density, Q is PV, σQ is PVS, θ is potential temperature, and $\dot{\theta}$ is the material rate of change of potential temperature. Because the vertical component of each flux contribution is zero (herein vertical refers to the direction normal to the isentropic surface), HM87 demonstrate that "there can be no net transport of PV across any isentropic surface". The terms on the right-hand side represent the advective and nonadvective flux components, respectively. The advective flux describes the movement of PVS (parallel to isentropic surfaces). Thus the divergence of the advective flux can only lead to changes in PVS magnitude akin to changing concentrations of a chemical tracer; sustained dilution can cause the concentration to approach zero but not change sign, and dilution in one location must be balanced by increased concentrations nearby. Divergence of the nonadvective flux behaves more like a system with sources and sinks, in which each local change is balanced by a nearby change of opposite sign. In section 3 we note that PV changes consistent with the advective flux (i.e., horizontal advection and convergence) appear to be present in Fig. 5, as well as changes associated with nonadvective fluxes (i.e., local cyclonic PV sources balanced by the emergence of anticyclonic PV nearby).

Although the flux form of the vorticity and PV equations is very useful for understanding global changes of vorticity or PV on isobaric or isentropic surfaces respectively, the physical mechanisms responsible for the changes, although implicit in the equations,[A1] are not as apparent. Expanding out the terms of the flux divergence helps identify these physical mechanisms. The expanded advective flux divergence,

$$\mathbf{u}_h \cdot [\nabla_h(\sigma Q)] + (\nabla \cdot \mathbf{u}_h)(\sigma Q), \quad \text{(A2)}$$

describes the horizontal advection and convergence of σQ. Assuming isentropic flow is near horizontal in Fig. 5, it would be expected that PVS will be advected by the horizontal flow, and in convective updrafts, where diabatic heating opposes adiabatic raising of isentropes, PVS magnitude will be enhanced in the convergent flow (low to mid troposphere) and weakened in the divergent flow above.

Vertical shear and diabatic heating are present in the convective updrafts of Fig. 5, which suggests the nonadvective flux in Eq. (A1) is nonzero. The divergence of this flux yields two terms,

$$\left(\frac{\partial \dot{\theta}}{\partial x}\frac{\partial v}{\partial \theta} - \frac{\partial \dot{\theta}}{\partial y}\frac{\partial u}{\partial \theta}\right) + \dot{\theta}\frac{\partial}{\partial \theta}\left(\frac{\partial v}{\partial x} - \frac{\partial u}{\partial y}\right). \quad \text{(A3)}$$

Recalling that in isentropic coordinates σQ takes the form $f + v_x - u_y$ (where the partial derivatives are taken on isentropic surfaces), Eq. (A3) can be expressed as

$$\left(\frac{\partial \dot{\theta}}{\partial x}\frac{\partial v}{\partial \theta} - \frac{\partial \dot{\theta}}{\partial y}\frac{\partial u}{\partial \theta}\right) + \dot{\theta}\frac{\partial}{\partial \theta}(\sigma Q). \quad \text{(A4)}$$

The first term in Eq. (A4) is mathematically analogous to the tilting term in the vorticity tendency equation (e.g., see Part I), and the second resembles vertical advection. Where vertical gradients of PVS exist the vertical movement of isentropes (relative to the fluid flow) associated with diabatic heating/cooling, will transport isentropes from a region of one PVS value to that of another. In the frame of reference of the isentropic surface this change describes a PV source or sink that resembles PV advection through the isentrope. Hence in Fig. 5, where vertical gradients of PV are negative in convective updrafts, a PV source will be evident that will resemble upward PV advection. HM87's flux representation implies that this source must be balanced by a compensating sink. The horizontal gradient of diabetic heating at the edge of the updraft tilts isentropic surfaces (relative to the fluid flow). Where isentropic-normal gradients of PV exist, isentropic-normal wind shear will typically be present, which implies the existence of isentropic-parallel vorticity. The tilting rotates isentropic surfaces such that the previously isentropic-parallel vorticity now contributes to isentropic normal vorticity (i.e., PV) on the newly tilted isentropic surface. This change in vorticity normal to the newly tilted isentropic surface is of opposite sign to the change associated with the vertical advection-like effect. In this way the tilting-like term [first term of Eq. (A4)] can provide a compensating PV sink (source) to the source (sink) associated with the vertical advection-like term. In section 3 we refer to these tilting and vertical advection analogues as tilting-like and vertical advection-like effects.

[A1] Olsson and Cotton (1997) also commented that although the local tendency of vertical vorticity is independent of a vertical flux divergence in the flux divergence form of the vertical vorticity equation, vertical advection is still implicitly represented.

REFERENCES

Arakawa, A., and W. H. Schubert, 1974: Interaction of a cumulus cloud ensemble with the large-scale environment, Part I. *J. Atmos. Sci.,* **31,** 674–701.

Bister, M., and K. A. Emanuel, 1997: The genesis of Hurricane Guillermo: TEXMEX analyses and a modeling study. *Mon. Wea. Rev.,* **125,** 2662–2682.

Dare, R. A., 2004: The BMRC Bulk Explicit Microphysics scheme. BMRC Research Rep. 99, 110 pp. [Available from the Bureau of Meteorology, GPO Box 1289K, Melbourne, VIC 3001, Australia.]

Davidson, N. E., and H. H. Hendon, 1989: Downstream development in the Southern Hemisphere monsoon during FGGE/WMONEX. *Mon. Wea. Rev.,* **117,** 1458–1470.

Gray, W. M., 1998: The formation of tropical cyclones. *Meteor. Atmos. Phys.,* **67,** 37–69.

Harr, P. A., R. L. Elsberry, and J. C. L. Chan, 1996: Transformation of a large monsoon depression to a tropical storm during TCM-93. *Mon. Wea. Rev.,* **124,** 2625–2643.

Haynes, P. H., and M. E. McIntyre, 1987: On the evolution of vorticity and potential vorticity in the presence of diabatic heating and frictional or other forces. *J. Atmos. Sci.,* **44,** 828–841.

Hendricks, E. A., M. T. Montgomery, and C. A. Davis, 2004: The role of vortical hot towers in the formation of Tropical Cyclone Diana (1984). *J. Atmos. Sci.,* **61,** 1209–1232.

Hoskins, B. J., M. E. McIntyre, and A. W. Robertson, 1985: On the use and significance of isentropic potential vorticity maps. *Quart. J. Roy. Meteor. Soc.,* **111,** 877–946.

Houze, R. A., 1997: Stratiform precipitation in regions of convection: A meteorological paradox? *Bull. Amer. Meteor. Soc.,* **78,** 2179–2196.

Jones, S. C., 1995: The evolution of vortices in vertical shear. I: Initially barotropic vortices. *Quart. J. Roy. Meteor. Soc.,* **121,** 821–851.

Keenan, T. D., J. McBride, G. Holland, N. Davidson, and B. Gunn, 1989: Diurnal variations during the Australian Monsoon Experiment (AMEX) phase II. *Mon. Wea. Rev.,* **117,** 2535–2553.

Kurihara, Y., and R. E. Tuleya, 1981: A numerical simulation study on the genesis of a tropical storm. *Mon. Wea. Rev.,* **109,** 1629–1653.

Melander, M. V., N. Zabusky, and J. McWilliams, 1988: Symmetric vortex merger in two dimensions: Causes and conditions. *J. Fluid Mech.,* **195,** 303–340.

Möller, J. D., and L. J. Shapiro, 2002: Balanced contributions to the intensification of Hurricane Opal as diagnosed from a GFDL model forecast. *Mon. Wea. Rev.,* **130,** 1866–1881.

Montgomery, M. T., and J. Enagonio, 1998: Tropical cyclogenesis via convectively forced vortex Rossby waves in a three-dimensional quasigeostrophic model. *J. Atmos. Sci.,* **55,** 3176–3207.

——, and G. Brunet, 2002: Vortex Rossby waves on smooth circular vortices. Part 2. Idealized numerical experiments for tropical cyclone and polar vortex interiors. *Dyn. Atmos. Oceans,* **35,** 179–204.

——, M. E. Nicholls, T. A. Cram, and A. B. Saunders, 2006: A vortical hot tower route to tropical cyclogenesis. *J. Atmos. Sci.,* **63,** 355–386.

Olsson, P. Q., and W. R. Cotton, 1997: Balanced and unbalanced circulations in a primitive equation simulation of a midlatitude MCC. Part I: The numerical simulation. *J. Atmos. Sci.,* **54,** 457–478.

Persing, J., and M. T. Montgomery, 2003: Hurricane superintensity. *J. Atmos. Sci.,* **60,** 2349–2371.

Puri, K., G. S. Dietachmayer, G. A. Mills, N. E. Davidson, R. A. Bowen, and L. W. Logan, 1998: The new BMRC Limited Area Prediction System, LAPS. *Aust. Meteor. Mag.,* **47,** 203–223.

Rapp, A. D., C. Kummerow, W. Berg, and B. Griffith, 2005: An evaluation of the proposed mechanism of the adaptive infrared iris hypothesis using TRMM VIRS and PR measurements. *J. Climate,* **18,** 4185–4194.

Ritchie, E. A., and G. J. Holland, 1997: Scale interactions during the formation of Typhoon Irving. *Mon. Wea. Rev.,* **125,** 1377–1396.

Simpson, J., E. A. Ritchie, G. J. Holland, J. Halverson, and S. Stewart, 1997: Mesoscale interactions in tropical cyclone genesis. *Mon. Wea. Rev.,* **125,** 2643–2661.

Tiedke, M., 1989: A comprehensive mass flux scheme for cumulus parameterization large-scale models. *Mon. Wea. Rev.,* **117,** 1779–1800.

Tory, K. J., M. T. Montgomery, and N. E. Davidson, 2006: Prediction and diagnosis of tropical cyclone formation in an NWP system. Part I: The critical role of vortex enhancement in deep convection. *J. Atmos. Sci.,* **63,** 3077–3090.

Wang, Y., and G. J. Holland, 1995: On the interaction of tropical-cyclone-scale vortices. IV: Baroclinic vortices. *Quart. J. Roy. Meteor. Soc.,* **121,** 95–126.